DISSOCIATION OF CARBON DIOXIDE IN ATMOSPHERIC PRESSURE MICROCHANNEL PLASMA DEVICES

BY

TAEGON OH

THESIS

Submitted in partial fulfillment of the requirements
for the degree of Master of Science in Materials Science and Engineering
in the Graduate College of the
University of Illinois at Urbana-Champaign, 2013

Urbana, Illinois

Adviser:

Professor J. Gary Eden

ABSTRACT

Plasma discharge of carbon dioxide at atmospheric pressure was successfully demonstrated in microchannel plasma devices at breakdown voltages lower than 1 kV_{RMS}. Optical emissions of molecular and ionic fragments of carbon dioxide were observed in emission spectra of visible wavelength range measured through a transparent dielectric coated with ITO electrode. Quantitative analysis by mass spectrometry derived the conversion rate of 2.40 ± 0.1 % and the energy efficiency of ~15 %. These results can be improved by modifying the device structures which leads to higher power loading and device packing density.

To my family

ACKNOWLEDGEMENTS

I am extremely grateful to God for his blessings and all he has planned for my life here. Through him, I could joyfully accomplish my graduate study on my own volition. I would like to give my biggest thank to my adviser, Professor J. Gary Eden, who supported this research and shared his insights with me. I cannot express my gratitude enough towards Professor Sung-Jin Park for his academic guidance on this project as well as his considerate advice during my personal struggle. Many thanks to all of former and current fellow researchers in the Laboratory for Optical Physics and Engineering for their kindness and willingness to help. My parents, aunt, grandmother, sister, and all other family members have consistently supported me despite the physical distance between us. I sincerely appreciate their continuous love, prayers, and faith.

TABLE OF CONTENTS

CHAPTER 1

INTRODUCTION

Global concern over the generation of greenhouse gases has been increasing over the past several decades. In particular, carbon dioxide is considered the largest contributor to global warming among heat-capturing gases. In 2009, carbon dioxide accounted for over 80 percent [1] of the greenhouse gases emitted in the United States. Carbon dioxide is mostly emitted by energy related issues such as electric power generation and fossil fuel engines for transportation, as a product of combustion reactions of carbon-containing compounds. Generation of 1 kWh of electricity produces 320 g of carbon dioxide by coal plants, 180 g by natural gas, and 240 g by gasoline [2]. Consequently, 5.5×10^9 tons of carbon dioxide is annually emitted by nation-wide power generation and transportation [2]. Dissociating and recycling carbon dioxide can be expected to allay global warming.

Large-scale chemical reduction of carbon dioxide could not only alleviate carbon dioxide emission, but could also provide a promising and affordable method of syngas production, as carbon dioxide is a cheap and abundant source of carbon. Different plasma systems have been devised to decompose carbon dioxide, such as dielectric barrier discharges [3, 4, 5], microwave discharges [6], and plasma jets [7]. Some researchers mixed carbon dioxide with methane and reformed the mixture to produce hydrogen, methanol, and other organic compounds [7].

In this study, decomposition of carbon dioxide at atmospheric pressure was performed in microplasma devices. Microplasma is non-equilibrium, low-temperature plasma generated inside features such as cavities and channels with characteristic dimensions ranging from 1 μm to 1 mm. One of the advantages of a microscopic system is that the breakdown voltage is reduced

for atmospheric pressure operation, which can be deduced from Paschen's law. Microplasmas have been noted for their high electron densities of ~10^{17} cm^{-3}, and electron temperatures of 1 – 5 eV [8]. These properties can be beneficial for chemical reactions involving carbon dioxide in that the destruction of carbon dioxide requires 5.5 eV of energy. As the size of channels and cavities is reduced, the ratio of volume to interface area decreases. Therefore, by scaling the dimensions down to the micro-range, we can achieve a large sheath region over the total volume.

CHAPTER 2

THEORETICAL BACKGROUND

2.1 DC Discharges

Plasma is often called the fourth state of matter in which molecules or atoms are partially ionized by providing sufficient energy. Both high pressure and temperature conditions can provide enough energy to reach thermodynamic equilibrium, but it is also possible to generate low-temperature, non-equilibrium plasmas with a sufficiently strong electric field. A DC discharge is the simplest model for a low-temperature plasma. In this type of discharge, an electric potential difference is applied between two parallel conductive plates. The gas medium breaks down to positively charged ions and electrons, which compose a small fraction of the total system. The charged particles transfer charges and energy by both diffusion and drift. The plasma sheath is an electron-depleted, positively charged region along the wall surface, which results from the difference in the thermal velocities of ions and electrons. The thermal velocity of a particle is related to the temperature and mass of the particle by $v \propto \sqrt{T/m}$. As the mass of an electron is ~10^{-5} of that for an ion, electrons move at least 100 times faster than ions. Electrons near the walls collide with and stick to the walls. Even though some electrons are lost in sheath, the quasi-neutrality of the bulk plasma remains applicable [9, 10].

Using Poisson's equation, the electric potential (Φ) and electron and ion density (n_e, n_i) can be related as Equation (2.1)

$$\frac{d^2\Phi}{d^2x} = -\frac{e}{\epsilon_0}(n_i - n_e) \tag{2.1}$$

where e is the elementary charge and ϵ_0 is the vacuum permittivity. Boltzmann's relation for electron and Taylor expansion reduce Equation (2.1) to

$$\Phi = \Phi_0 \, exp\left(-\frac{|x|}{\lambda_{De}}\right) \tag{2.2}$$

with definition of electron Debye length λ_{De}.

$$\lambda_{De} = \sqrt{\frac{\epsilon_0 T_e}{e n_0}} \tag{2.3}$$

Electron Debye length is generally used as the characteristic length scale in plasmas. It is also related to another important parameter, the electron plasma frequency (ω_{pe}), which is a measure of the frequency of plasma oscillation. It can be derived from Gauss's law (derivation omitted).

$$\omega_{pe} = \sqrt{\frac{e^2 n_0}{\epsilon_0 m}} \tag{2.4}$$

$$\lambda_{De} = \frac{v_{thermal}}{\omega_{pe}} \tag{2.5}$$

A representative potential profile resulting from the formation of the plasma sheath is shown in Figure 2.1. In this plot, x = 0 is defined as the sheath edge, where $n_i = n_e = n_s$ and $\Phi = 0$.

The simplest model for the high voltage sheath is the matrix sheath. Two assumptions within the sheath region are required for the approximation: high sheath voltage (with respect to electron energy) and a constant ion density ($n_i = n_s$). When a very high voltage (relative to T_e) is applied, the electric potential at the sheath is much lower than at the bulk plasma-sheath boundary. Therefore, the electron density, n_e, becomes negligible (Boltzmann's relation). The electric potential can be obtained from Maxwell's equation ($\epsilon_0 \nabla \cdot \vec{E} = \rho$):

$$\Phi = -\frac{e n_s}{\epsilon_0} \cdot \frac{x^2}{2}. \tag{2.6}$$

When $x = s$ (wall interface), $\Phi = V_{cat}$, the voltage of the cathode with respect to the sheath edge potential. Thus,

$$s = \lambda_{De}\sqrt{\frac{2V_{cat}}{T_e}} \tag{2.7}$$

Equation (2.7) gives an approximation of the sheath thickness to be a few tens of electron Debye lengths.

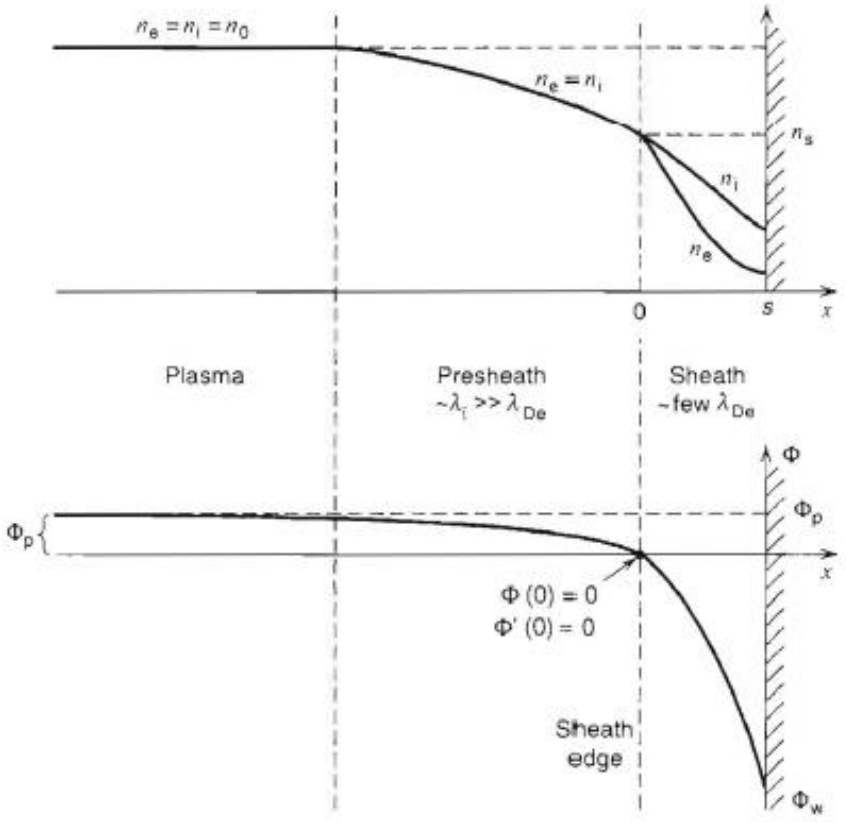

Figure 2.1. Qualitative plot of electric potential through sheath and presheath region near the wall. The sheath edge is at x = 0 and it is the boundary between quasi neutral presheath and positively charged sheath. [9]

2.2 Microplasma

Microplasma is low-temperature, non-equilibrium plasma, the dimensions of which are less than 1 mm. Microplasmas have several advantages over macroscopic plasma systems. High electron densities of up to 10^{17} cm^{-3} have been reported for microplasmas [8]. This value is several orders of magnitude higher than conventional low-temperature low-pressure plasmas, and even close to the carrier concentration of semiconductors.

Obeying Paschen's law, the breakdown voltage can be lowered, which implies that plasma can be operated stably even above atmospheric pressure. Paschen's curve can be derived from the Townsend ionization coefficient (α) and the Townsend formula. It describes the relationship between the avalanche breakdown voltage (V) and the product of pressure and the plane gap (pd) [10].

$$V = \frac{B(pd)}{ln(Apd) - ln[ln(1 + 1/\gamma)]} = \frac{B(pd)}{C + ln(pd)} \tag{2.8}$$

where A, B and C are numerical parameters, which are different for each gas, γ is the secondary electron emission coefficient. Paschen's curves for several molecular gases are plotted in Figure 2.2. At certain pressure above a few Torr, reducing the plane gap to micrometer range lowers the breakdown voltage. For example, when $p = 760$ Torr of carbon dioxide, above 40 kV must be applied for a discharge in a 1 cm plane gap, whereas 1 kV is calculated to be enough for 100 μm microplasmas.

Another advantage of scaling down the characteristic dimension of plasma devices is a larger surface-area-to-volume ratio. Rather than having the bulk plasma solely determine the characteristics, the sheath region takes a bigger role in determining the characteristics of the plasma. Also, the wall interaction becomes more significant as the surface-area-to-volume ratio

increases. The gas temperatures of ~500 K was achieved due to the large heat transfer afforded by an increased wall-plasma interface area [8]. Some chemical reactions can be catalyzed by the surface, such as three body recombination reactions or decomposition reactions [11]. Microplasmas are especially promising in that the intermediate state of carbon dioxide decomposition reaction includes oxygen atoms that can be stabilized on ceramic surfaces.

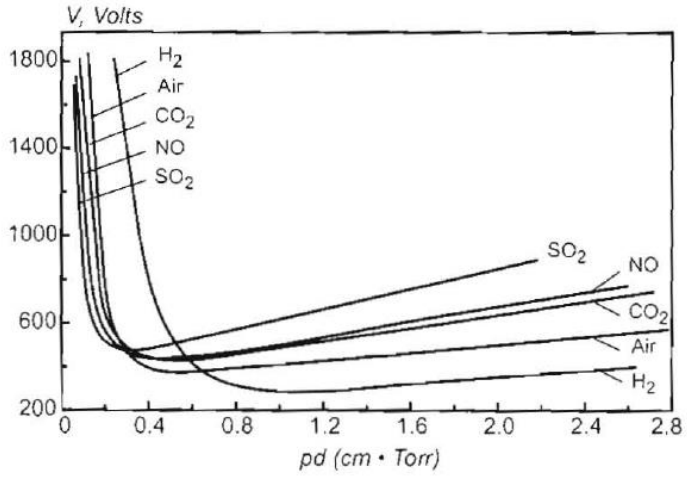

Figure 2.2. Paschen's curve for different molecular gases. For carbon dioxide, A = 20 $cm^{-1}Torr^{-1}$ and B = 466 V $cm^{-1}Torr^{-1}$ [10].

2.3 CO_2 Plasma and Dissociation Reactions

The chemical decomposition reaction of carbon dioxide can be summarized as below.

$$CO_2 \rightarrow CO + \frac{1}{2}O_2, \qquad \Delta H = 2.9\ eV/mol \tag{2.9}$$

The rate-determining step of this reaction is the bond breaking reaction of the C-O double bond into carbon monoxide and atomic oxygen. The oxygen atom then recombines with another oxygen atom or detaches an oxygen atom from a carbon dioxide molecule [12]:

$$CO_2 \rightarrow CO + O, \qquad \Delta H = 5.5\ eV/mol \tag{2.10}$$

$$O + O \rightarrow O_2, \qquad \Delta H = -5.15\ eV/mol \tag{2.11}$$

$$O + CO_2 \rightarrow CO + O_2, \qquad \Delta H = 0.3\ eV/mol \tag{2.12}$$

There are several possible mechanisms of carbon dioxide dissociation. The dissociative attachment of an electron produces carbon monoxide and an oxygen anion.

$$e^- + CO_2 \rightarrow CO + O^- \tag{2.13}$$

The maximum cross section is negligible (10^{-18} cm^2) compared to other mechanisms. When the electron energy is higher than 5 eV, electron impact is effective for electronic excitation of carbon dioxide molecules resulting in dissociation.

$$e^- + CO_2(^1\Sigma^+) \rightarrow CO(a^3\Pi) + O(^3P) \tag{2.14}$$

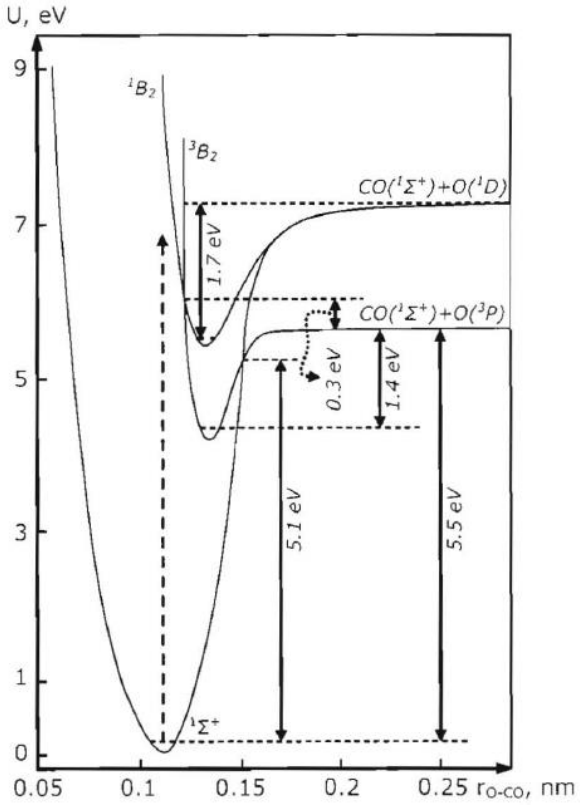

Figure 2.3. The energy levels of $CO_2(^1\Sigma^+)$ and dissociation products, CO and O, showing dissociation mechanism by vibrational excitation from electron impact. CO_2 dissociate directly or through adiabatic/non-adiabatic transitions. [10]

Vibrational excitation is the most effective mechanism for the CO_2 dissociation in non-thermal plasmas in which $T_e \sim 1$ eV. The electrons with this energy easily excite carbon dioxide molecules by electron impact excitation, and vibrational-translational relaxation is much slower by several orders of magnitude [10]. Therefore, significant populations of $CO_2(^1\Sigma^+)$, ground electronic state and $^1\Sigma^+$ vibrational state, can be achieved. Higher vibrational levels can be reached by vibrational-vibrational relaxation. Highly excited molecules with enough energy (ΔH) dissociate by Equation (2.11), and others can follow either adiabatic (Equation (2.15)) or non-adiabatic (Equation (2.16)) transitions leading to dissociation.

$$CO_2^*(^1\Sigma^+) \rightarrow CO(^1\Sigma^+) + O(^1D) \tag{2.15}$$

$$CO_2^*(^1\Sigma^+) \rightarrow CO_2^*(^1B_2) \rightarrow CO(^1\Sigma^+) + O(^3P) \tag{2.16}$$

The energy diagram plotted in Figure 2.3 describes well these reactions.

CHAPTER 3

EXPERIMENTAL METHODS

3.1 Device Fabrication

The design and fabrication of microchannel plasma devices were the most important part of this research as the material properties of dielectric layers and the dimensions of discharge volume determine the characteristics of plasmas. Selecting dielectric materials, scaling down the dimensions of cavities/channels, designing device structures, and developing fabrication techniques have been studied by former and current researchers at the Laboratory for Optical Physics and Engineering. Nanoporous anodic aluminum oxide (alumina) was grown by an electrochemical oxidation process and was used as a dielectric barrier material for this experiment. Nanostructured anodic alumina showed its superiority as a dielectric material in plasma devices in that even with thin dielectric thicknesses, alumina microplasma devices can withstand atmospheric pressure microplasma discharge with continuous and stable operation [13]. Soda-lime glass was also used as a dielectric material for its abundance, optical transparency, and robustness.

Our microchannel plasma devices for carbon dioxide dissociation were composed of two dielectric pieces: one having channels and the other covering the channels. Four combinations were able to be fabricated with these two dielectric materials: glass-glass (GG), glass-alumina (GA), alumina-glass (AG), and alumina-alumina (AA).

Three major steps were performed to fabricate these microchannel plasma devices: 1) preparing the dielectric substrate, 2) etching the channels, and 3) combining the two dielectrics into one device. The nanoporous aluminum oxide was grown by electrochemical anodization.

Aluminum sheets (99.999 % Al) having thicknesses of 100, 250, or 500 μm were cut into 2×10 cm^2 segments and flattened by heat-treatment at 500 ℃ for 1 hour under pressure. Then, the aluminum pieces were anodized in 0.3 M oxalic acid by 70 VDC for 1 hour and 100 VDC for varying lengths of time. We varied the duration of the latter process to control the thickness of oxide layer. The oxide thickness is plotted by the total process time in Figure 3.1. As the technique has been used for many decades, the chemistry of anodization and material properties of anodic alumina are well known [13, 14].

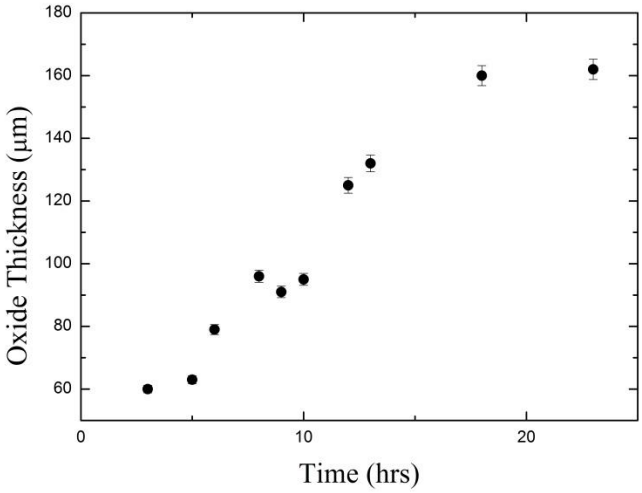

Figure 3.1. The oxide thickness as a function of anodization time. The thickness has an upper limit, occurring when the reaction rates for the growth and dissolution of oxide layer equalize.

Having embedded aluminum as an electrode, anodic aluminum substrate did not need an additional step for electrode preparation. However, a conductive layer should be deposited on the soda-lime glass substrate. 150 nm thick film of tin-doped indium oxide (ITO), which is a well-known transparent conductive oxide, was deposited on 400 μm thick soda-lime glass by sputtering, and it enabled observation and optical analysis through the electrode and the substrate. A chromium-nickel electrode having a thickness of 200 nm was deposited by e-beam evaporation on the devices for experiments other than optical measurements.

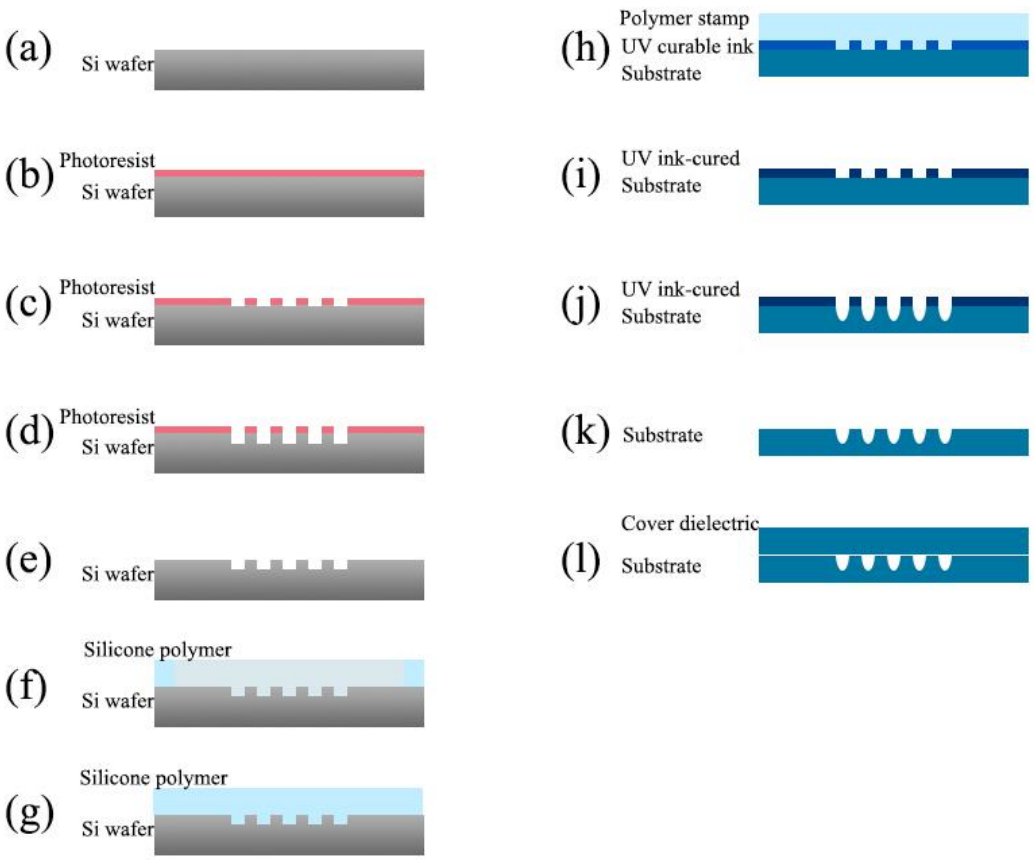

Figure 3.2. Schematic diagram for masking and etching process by micropowder ablation technique: (a)-(e) photolithography and ICP-RIE making master wafer, (f)-(g) replication of polymer stamp, (h)-(i) mask substrate with UV curable elastic ink, (j)-(k) etching by micropowder ablation, and (l) completed device

Once the dielectric substrate was prepared, the channels were etched by micropowder ablation, Figure 3.2. Before micropowder ablation could be performed, an etch-mask must be fabricated. To do this, photoresist was first spin-coated on a silicon wafer and patterned by photolithography. Inductively coupled plasma reactive-ion etching (ICP RIE) was used to make channels with a depth of ~50 μm and a width of 200 μm on the silicon wafer. After the photoresist layer was removed, the master wafer was treated in Repel Silane (dimethyldichlorosilane by GE Healthcare) for 20 minutes to reduce hydrophilicity so that silicone polymer stamp can be removed easily. RTV615 (by GE Healthcare), flexible silicone

rubber which is transparent to ultraviolet down to a wavelength of 250 nm, was poured onto the master wafer. The polymer was vulcanized after 1 hour of heat curing at 80 ℃, and when the polymer was peeled off, the microchannel patterns were embossed on the polymer stamp. After this, the substrate surface was covered with ultraviolet curable polymer (GEC-10H by Jujo Chemical), and the pattern on the transparent polymer stamp was transferred to the surface by imprinting. Then, the substrate and stacked polymer complex were cured under 400 W ultraviolet lamp for 3 minutes. When the transparent polymer stamp was physically removed, the elastic masks of 50 μm thickness remained with patterns on the substrate.

Micropowder ablation is an etching technique for brittle materials. It can etch amorphous substrates with high aspect ratios, which cannot be achieved in these materials by wet etch or reactive ion etches [15]. In this instrument, micro-sized powder is carried by high-pressure dry gas and blown onto the target substrate. The particles transfer momentum to the substrate surface and cause the substrate to be abraded into particles having sizes similar to the powder. Continuous uniaxial blowing etches cavities/channels of high aspect ratio into the substrate. The cross-sections of the etched features show a roughly quadratic profile because the momentum transferred to the substrate is dependent on the incident angle of the particles [15, 16]. The micropowder was sprayed at an angle perpendicular to the substrate through a 3.85 mm × 0.325 mm nozzle which was fixed at 25 mm above the target substrate. The nozzle was controlled to move along the channels at 0.76 mm/s. Al_2O_3 powder of 5 μm diameter was used and the gas pressure was set to 300 kPa. The etch depth was controlled by the number of sweeps along the channel. Figure 3.3 and 3.4 are scanning electron microscope images of channels in soda-lime glass and anodic aluminum substrates.

After the channels were etched on substrates, they were covered by another dielectric piece, either glass or alumina. Soda-lime glass having a thickness of 400 μm covered with ITO or chromium as an electrode was used as the top dielectric-electrode. 100 μm of aluminum oxide was grown on aluminum and was also used as another dielectric cover for the channels.

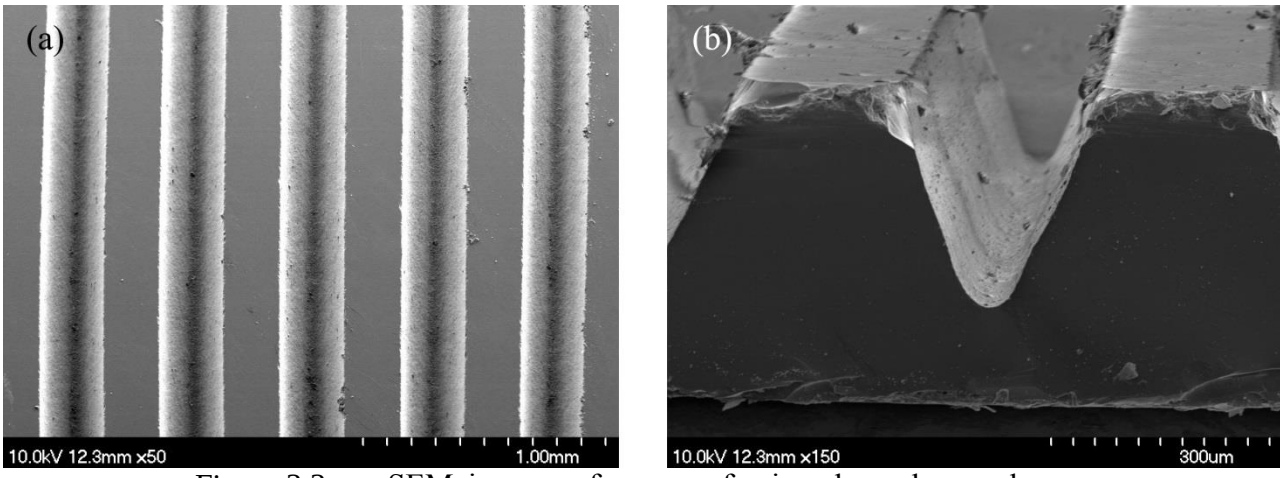

Figure 3.3. SEM images of arrays of microchannels on glass etched by powder blasting (a) top view (b) cross-section.

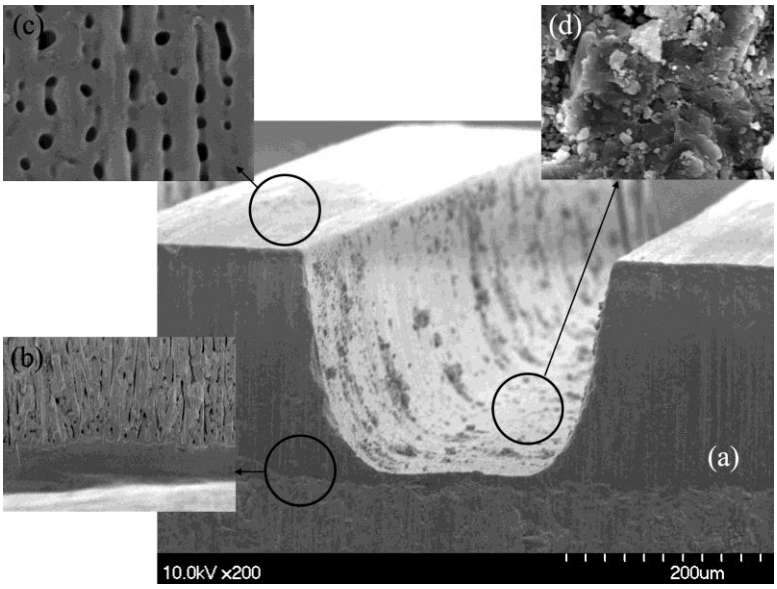

Figure 3.4. SEM images of microchannels on alumina (a) cross section (b) magnified cross section (c) substrate surface (d) channel bottom. Nanostructures of less than 100 nm can be observed in (b) and (c). Channel bottom has rough surface because of collisional fracture.

3.2 Gas Feed and Measurement Setup

Precise control of gas injection into plasma devices is critical for a plasma chemistry experiment. A vacuum chamber with gas flow control was built for both low pressure experiments and atmospheric pressure flow experiments, and is drawn schematically in Figure 3.5. Starting from each gas tank, the gas lines are connected to a mass flow controller, followed by a solenoid valve. The manifold connected to the valves has two exit ports: one leads

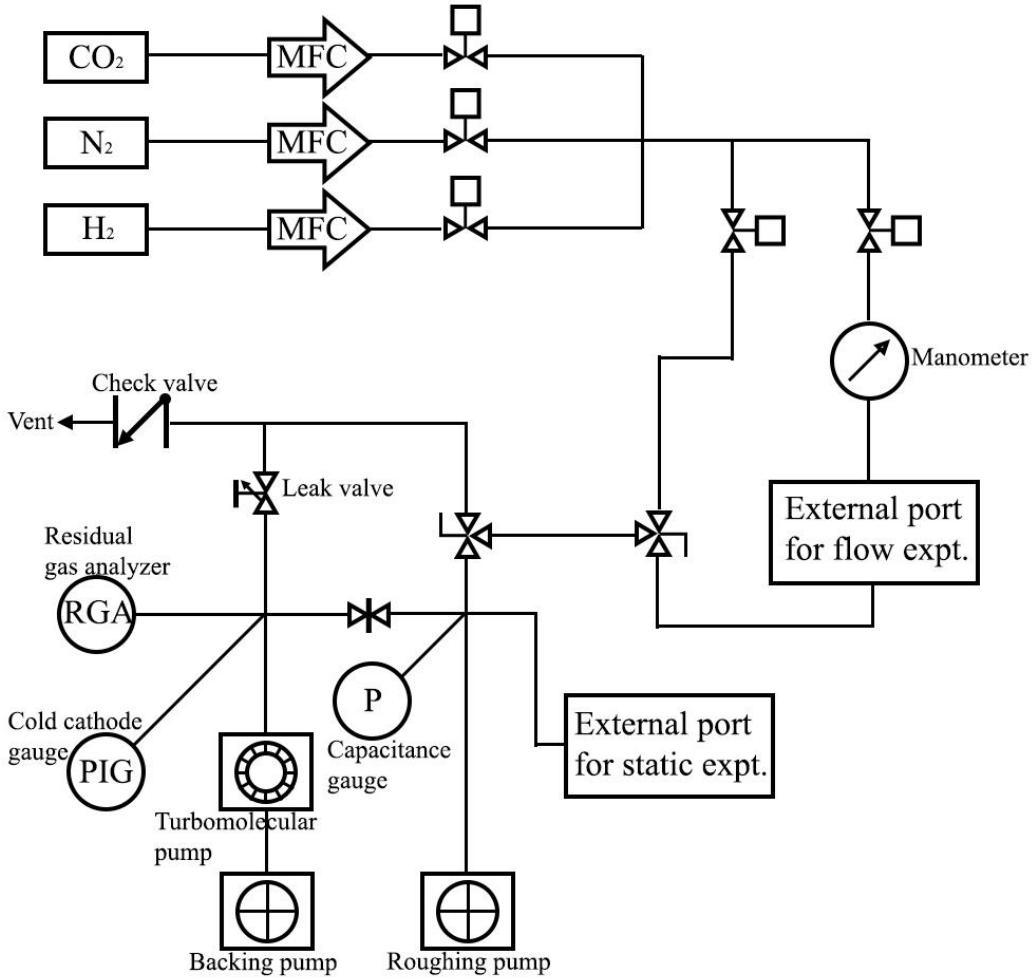

Figure 3.5. Schematic description of gas input and vacuum chamber for flow experiment and analysis.

to the vacuum chamber directly, and the other leads to an external connector for a device. The former feeds pure or mixed gases to the chamber at a certain pressure, monitored by a capacitance manometer. The latter is for atmospheric pressure flow experiments, and provides pure or mixed gases to a microchannel device at a constant gas flow rate. The gas coming out of the device is collected again for analysis. The first three-way ball valve determines which gas to receive, input gas or output gas, and the second valve controls where the gas is sent, either to the chamber or to a bypass line leading to a high vacuum pipe. The bypass line includes a leak valve that controls the leak rate as low as 7.5×10^{-7} Torr-L/s, which can maintain constant flow from atmospheric pressure to high vacuum. The gases sampled by the bypass line into the high vacuum chamber can be analyzed both quantitatively and qualitatively by a residual gas analyzer, which is a type of quadrupole mass spectrometer. Excess sampled gases flew out to venting line after passing through a check valve.

Low-pressure experiments were available as well since the vacuum chamber has an external port. After loaded, the device was pumped down to $< 10^{-7}$ Torr for more than 12 hours to remove the adsorbed impurity molecules on substrate surfaces. Then, the chamber was isolated from the high vacuum pipe by a gate valve, and gas was introduced into the chamber to fill it to the desired composition and pressure. A 20 kHz AC voltage was applied to the top and bottom electrodes of the microplasma devices.

Observation and optical measurement were performed through devices with a transparent electrode (ITO) and glass dielectric. Optical emission spectra were recorded through the transparent layers of this type of device. Though ITO-glass showed ~80 % transmittance throughout the visible portion of the spectrum, UV light having shorter wavelength than 400 nm was attenuated significantly and the measurement in this range can be affected (Figure 3.7).

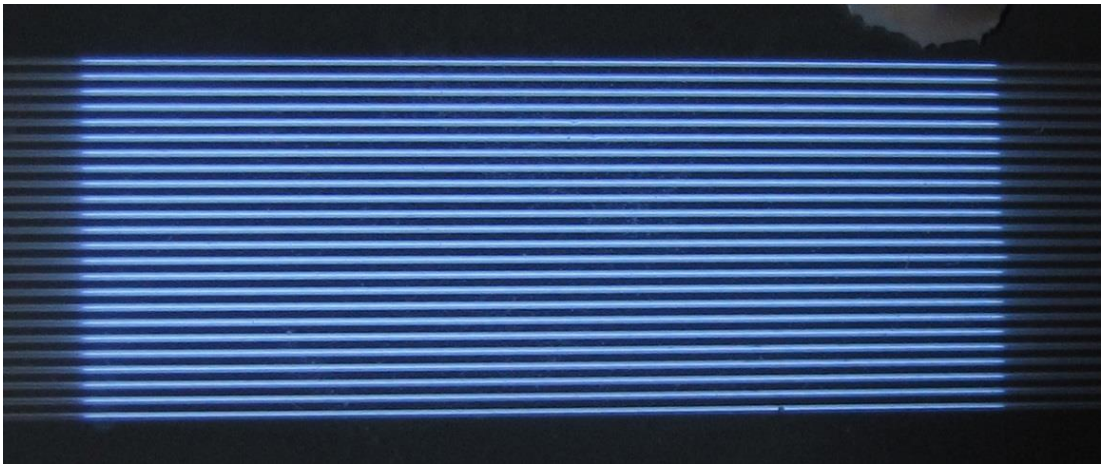

Figure 3.6. Operation of an array of 24 microplasma channels. The width and depth of each channel is 200 μm and 300 μm, respectively, and the interchannel distance is 500 μm. 0.2 slm of CO_2 is flowing, and 2.0 kV_{rms} is applied.

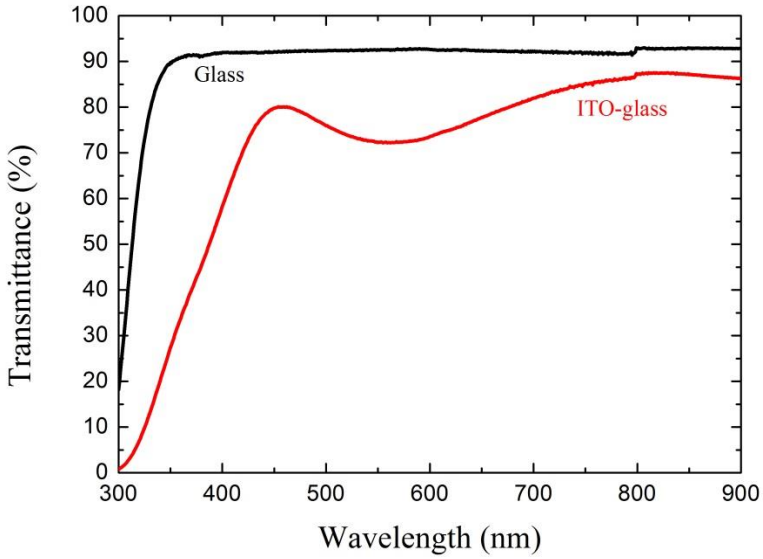

Figure 3.7. Transmittances of soda-lime glass and ITO-coated-glass in visible range. Blue – UV lights (300 – 400 nm) are significantly attenuated.

CHAPTER 4

RESULTS AND DISCUSSION

4.1 Dielectric Selection

As mentioned in Chapter 3, four different types of devices were fabricated: glass-glass (GG), glass-alumina (GA), alumina-glass (AG), and alumina-alumina (AA). The acronyms indicate the dielectric materials of a device – the first letter to the channel side, and the second to the cover material. Each type of devices were fabricated and then compared by stability of operation and breakdown voltage. 6 microchannels were etched to 300 μm in depth on 400 μm thick soda-lime glass (Figure 3.3), leaving a 100 μm dielectric barrier to maintain mechanical stability. A nanoporous aluminum oxide layer was grown to 200 μm, and 6 channels with depth of 160 μm were etched from the alumina layer. Although the channels on each dielectric had different depth, the cross-sectional areas were measured to be same (Figure 3.3 and 3.4). The width of the microchannels on both dielectrics was controlled to 200 μm. The cover dielectric was either soda-lime glass having a thickness of 400 μm or aluminum oxide having a thickness of 100 μm. Pure carbon dioxide was flowed through the devices at the flow rate of 200 sccm.

An IV curve was obtained for each device (Figure 4.1). The breakdown voltages can be calculated from the curves using the intersection of two linear fittings before and after breakdown. The results of calculations were recorded in Table 4.2. The alumina-alumina, glass-alumina, and alumina-glass devices had turn-on voltages ranging from 0.90 kV_{RMS} to 1.6 kV_{RMS}. The devices made of soda-lime glass top and bottom dielectrics did not breakdown in the voltage range we tested. This result can be explained by the dielectric thicknesses. Assuming simple series capacitors, the breakdown voltage can be represented by Equation (4.1).

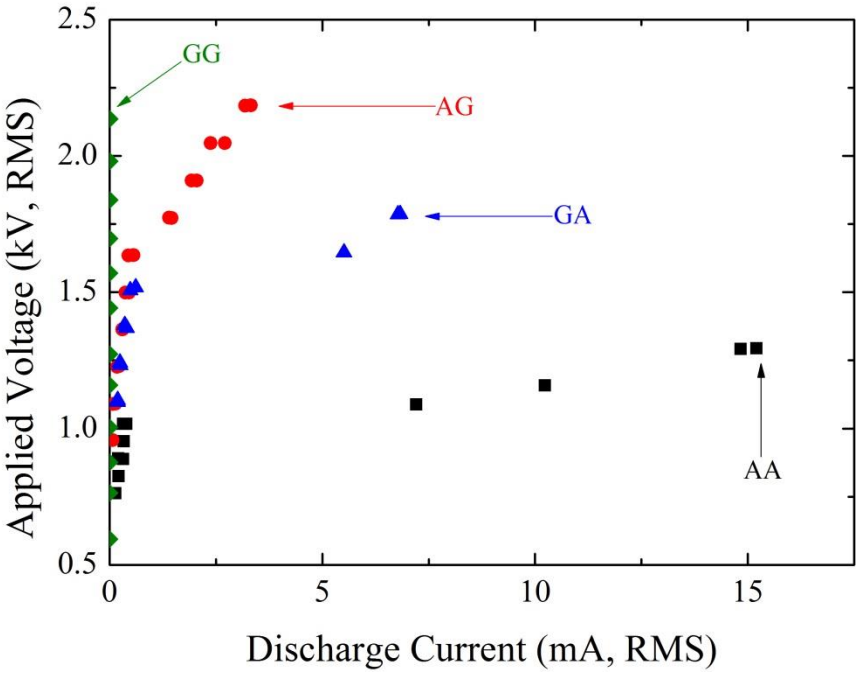

Figure 4.1. IV curve for each type of devices, 20 kHz AC power, with 200 sccm of CO_2 flow. The discharge current jumps up after breakdown. The devices were operated successfully except for glass-glass devices.

Table 4.1. Material properties for soda-lime glass (from manufacturer) and nanoporous anodic aluminum [17, 18]

Materials	Soda-Lime Glass	Nanoporous Alumina
Dielectric Strength (MV/cm)	9 – 13	7 – 10
Relative Permittivity at 25°C	7.7 ± 0.1	10.5 ± 0.27
Young's Modulus (GPa)	70 ± 2	200 ± 11
Softening Temperature (°C)	575	m.p. > 2000
Thermal Conductivity W/m-K)	0.94	20 – 30
CTE at 25°C (α, 10^{-6} /K)	9	6.55

Table 4.2. The breakdown voltages of the four types of devices.

Device	V_{br} (kV, RMS)	$\Sigma\ (d/\epsilon_r)$
Alumina-Alumina	0.90	13
Glass-Alumina	1.1	23
Alumina-Glass	1.6	56
Glass-Glass	-	65

$$V_{br} = V_{br,0}\left(\frac{\epsilon_{r,gas}}{d_{gas}}\sum_i\left(\frac{d_i}{\epsilon_{r,i}}\right)+1\right) \quad (4.1)$$

where $\epsilon_{r,gas}$ and d_{gas} are the relative permittivity and thickness of gas layer, $\epsilon_{r,i}$ and d_i are those of top and bottom dielectric layer, and $V_{br,0}$ is the breakdown voltage without dielectric layers. The linear dependence of V_{br} on $\sum_i(d_i/\epsilon_{r,i})$ was observed in our experiment (Table 4.2). The alumina-alumina device, having thinnest dielectric layers, had the lowest breakdown voltage. The stability of each device was also tested. Alumina-alumina devices were able to be operated stably at 6 W of discharge power for at least several hours. Alumina-glass devices could also withstand for hours, but the power loading was much lower because of the thick dielectric layers and the low discharge current. Glass-alumina devices failed (electric short and burn) after 2 minutes of operation at about 7 W of discharge power, and the joule heating of the dielectric layers was found to be the cause of the failure. As the temperature increases, the thermal expansion mismatch incurs strain in the substrates, especially to the bottom of microchannels on glass substrate. The alumina-alumina devices did not fail because both top and bottom dielectric layers had high thermal conductivity and were relatively resilient to heat. The current flow of alumina-glass devices was not sufficiently high to cause heat confinement and thermal strain.

Figure 4.2. Optical microscope image of failed glass-alumina device

Although air cooling made decomposition of CO_2 less favorable (heat favors decomposition [10, 19]), it enabled stable and continuous operation of the devices. For the high power loading and the stability, alumina-alumina devices and glass-alumina devices were chosen for further experiments and analyses.

4.2 Optical Emission Spectroscopy

The optical emission spectrum of carbon dioxide was measured with a glass-alumina device having an ITO electrode on glass substrate (Figure 3.6). The information on the peak shown at the spectrum was found in references [19, 20, 21, 22]. The peak assignments are listed in Table 4.3.

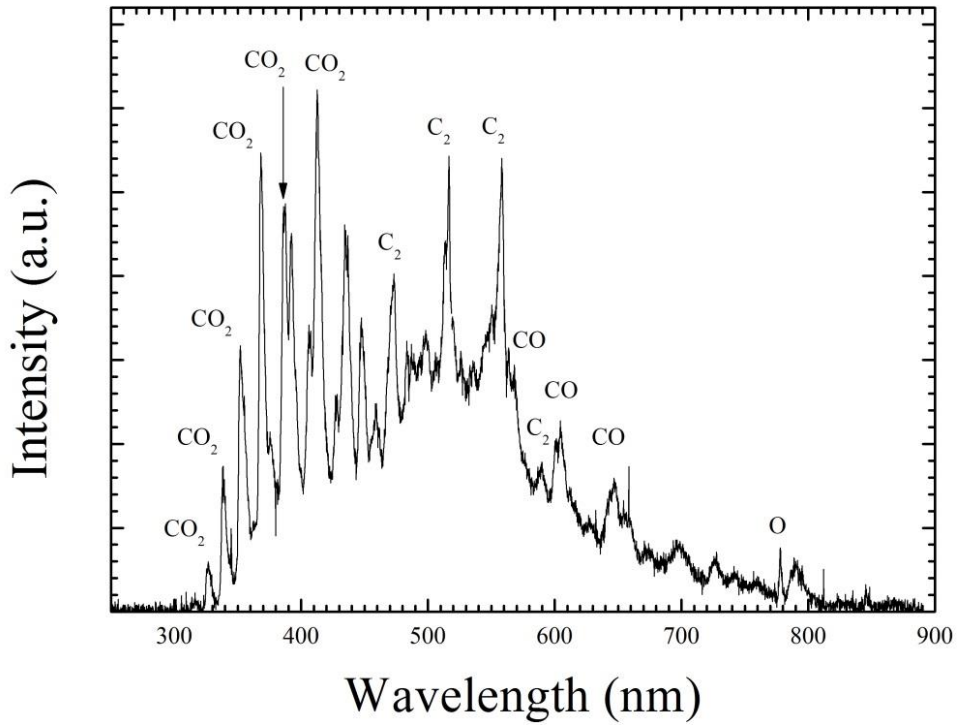

Figure 4.3. Optical emission spectrum of CO_2 microplasma discharge. 200 sccm of CO_2, 780 Torr inlet, V_{p-p}=5.5 kV

Table 4.3 Peak assignments for CO_2 microplasma, Figure 4.3 [19, 20, 21, 22].

Species	Peak position (nm)	Transition
C_2	471.5	Swan system, $A^3\Pi_g \rightarrow B^3\Pi_u, \Delta v = 1$
	516.5	Swan system, $A^3\Pi_g \rightarrow B^3\Pi_u, \Delta v = 0$
	558.5	Swan system, $A^3\Pi_g \rightarrow B^3\Pi_u, \Delta v = -1$
	589.9	High pressure bands, $A^3\Pi_g \rightarrow B^3\Pi_u, v' = 6 \rightarrow v'' = 8$
CO	458.6	the Triplet bands, $d^3\Pi \rightarrow a^3\Pi, v' = 6 \rightarrow v'' = 0$
	564.8	the Triplet bands, $d^3\Pi \rightarrow a^3\Pi, v' = 2 \rightarrow v'' = 0$
	601.0	the Triplet bands, $d^3\Pi \rightarrow a^3\Pi, v' = 1 \rightarrow v'' = 0$
	643.3	the Triplet bands, $d^3\Pi \rightarrow a^3\Pi, v' = 0 \rightarrow v'' = 0$
CO^+	427.4	Comet-tail system, $A^2\Pi \rightarrow {}^2\Sigma$ (gs), $v' = 2 \rightarrow v'' = 0$
CO_2 and CO_2^+	326.5	Fox, Duffendack and Barker's System
	337.8	
	369.2	
	387.1	
	412.1	
N_2	405.9	Second positive, $C^3\Pi \rightarrow B^3\Pi, v' = 0 \rightarrow v'' = 3$
	434.4	Second positive, $C^3\Pi \rightarrow B^3\Pi, v' = 0 \rightarrow v'' = 4$
N_2^+	391.4	First negative, $B^2\Sigma_u^+ \rightarrow X^2\Sigma_g^+, v' = 0 \rightarrow v'' = 0$
O	777	Atomic transition, ${}^5P \rightarrow {}^5$
O_2^+	351.8	Second negative, ${}^2\Pi \rightarrow {}^2\Pi$

The C_2 Swan bands at 472, 516, and 558 nm are well-known for many plasma systems, including carbon dioxide [20, 21]. The C_2 high pressure band at 590 nm is not usually observed in comparable atmospheric carbon dioxide plasmas, but in moderate pressure carbon monoxide discharges. The appearance of the C_2 high pressure bands and the atomic oxygen peak at 777 nm imply that significant amount of destruction of C-O double happened inside our microplasma devices. Also, particularly in this study, many carbon dioxide and carbon dioxide cation peaks were also observed in 300 – 400 nm range. These peaks were known to appear in negative glow discharges, such as a hollow cathode [20]. Series of the CO triplet bands indicated that carbon dioxide was decomposed mostly into carbon monoxide and oxygen. The appearances of some peaks from transitions of molecular ions (CO_2^+, CO^+, and O_2^+) were also noted. If the mechanism is presumed to be electron-impact ionization, it can be deduced that some of the free

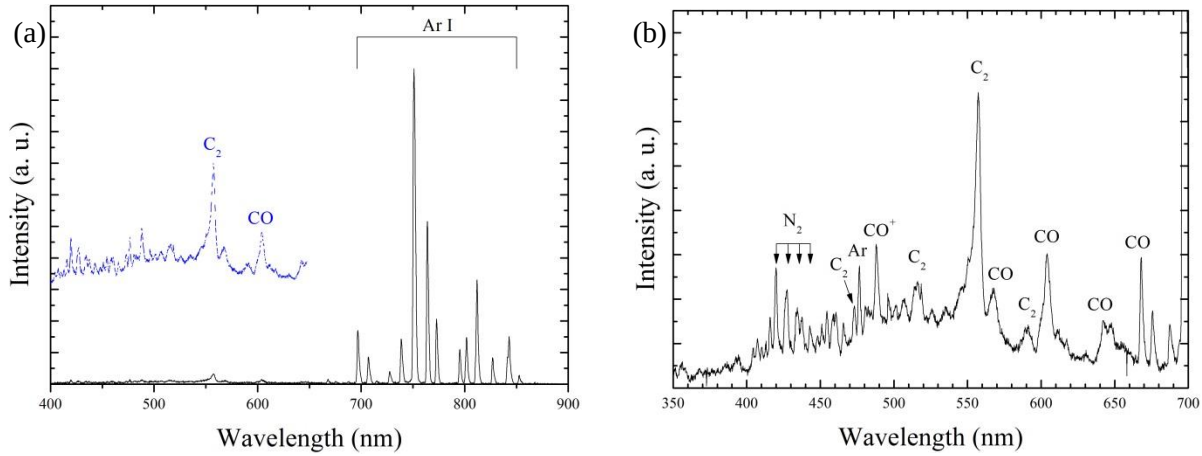

Figure 4.4. The optical emission spectrum of 70 % Ar – 30 % CO_2 microplasma discharge, V_{p-p}=5.5 kV

electrons in microplasmas have energies greater than 12 – 14 eV, which is the range of ionization energies of the molecules [23]. Further experiment is needed to suggest mechanisms and to measure the electron density and temperature.

In addition, the optical emission spectrum of Ar-CO_2 mixture plasma was measured. The most intense peaks were argon atomic lines (700 – 900 nm, Figure 4.4 (a)), and the peaks of carbon-related compounds also appeared in 500 – 600 nm range (Figure 4.4 (b)). The C_2 Swan

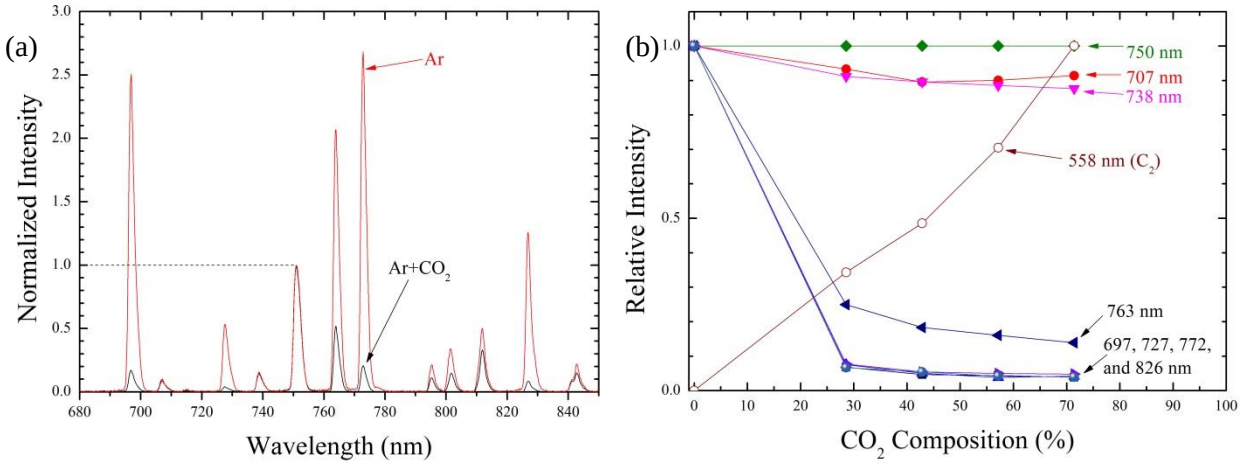

Figure 4.5. (a) Comparison of peak heights of optical emission spectrua of pure Ar plasma (red) and 70 % Ar – 30 % CO_2 (black). (b) Relative normalized peak intensities plotted by different CO_2 composition.

band at 558 nm was much more intense than the other two at 472 and 516 nm, whereas the intensities of the three peaks were comparable to each other in the emission spectrum of a pure CO_2 microplasma in Figure 4.3.

The intensities of the argon atomic lines also differed from those of the pure argon microplasma optical emission spectrum. In Figure 4.5 (a), the spectra were normalized to a peak at 750 nm which was the highest peak in Ar-CO_2 mixture discharge, and some inversions of relative intensities of some peaks were observed. For example, a peak at 750 nm was the strongest in the mixture and the peaks at 697, 763, and 772 nm were much higher than that at 750 nm in pure argon spectrum. The peak intensities were plotted against carbon dioxide compositions in Ar-CO_2 mixture (Figure 4.5 (b)). Most of the peaks decreased significantly with increasing CO_2 composition, but the peaks at 750, 707, and 738 nm did not decrease much.

The optical emission spectra of Ar-CO_2 mixture plasma suggest a Penning excitation mechanism from a certain energy level of argon to a C_2 excited state. The transitions whose peak intensity decreased dramatically (696, 727, 772, and 826 nm) were from argon $^2P^0_{1/2}$ (4p singlet state), whereas the two peaks at 707 and 738 nm appeared by transitions from $^2P^0_{3/2}$ (4p triplet state) [22]. It can be assumed that the addition of carbon dioxide resulted in population changes in the argon excited states, and consequently the peak intensity ratios. Another possible explanation is that the characteristics of the plasma, such as electron density and temperature, could have been affected by the addition of carbon dioxide, and they caused the relative changes of peak intensities. Quantitative and mathematical analysis of higher resolution spectra should be performed to reveal the reason for the intensity inversions.

4.3 Conversion Rate and Energy Efficiency

The quantitative measurement of gas compositions was recorded with a quadrupole mass spectrometer. The conversion rate (α, %) is a measure of the amount of carbon dioxide converted into other compounds. It can be calculated by Equation (4.2).

$$\alpha\ (\%) = \frac{C_{CO_2,initial} - C_{CO_2,product}}{C_{CO_{2,initial}}} \tag{4.2}$$

where $C_{CO_2,initial}$ and $C_{CO_2,product}$ are the concentrations of carbon dioxide in the input and product gases, respectively. The energy yield (E_y) is often used to indicate the amount of carbon dioxide decomposed per unit power [24]. It can be calculated by Equation (4.3) with appropriate unit conversions for our system.

$$E_y(g/kWh) = \frac{\alpha \dot{m}}{P} \tag{4.3}$$

where $\dot{m}$ is the mass flow rate of the inlet CO_2 , and P is the power supplied to the devices. The energy efficiency (η) is the portion of the energy consumed by the dissociation reaction of carbon dioxide into carbon monoxide over the total energy consumed [10]:

$$\eta(\%) = \frac{\Delta H}{E_{CO}} \tag{4.4}$$

Here, E_{CO} is the energy consumed by the system to destruct one mole of carbon dioxide and form the same amount of carbon monoxide. ΔH is the specific heat of reaction in Equation (2.9). The energy efficiency can reach up to 90 % using non-equilibrium microwave discharges in supersonic flow at moderate pressure [10]. The energy efficiency can be represented as a function of mass flow rate of inlet CO_2 ($\dot{m}_{CO_2}$) and conversion rate (α).

$$\eta(\%) = \alpha \frac{\dot{m}_{CO_2}}{\mu_{CO_2}} \frac{2.9}{P} \tag{4.5}$$

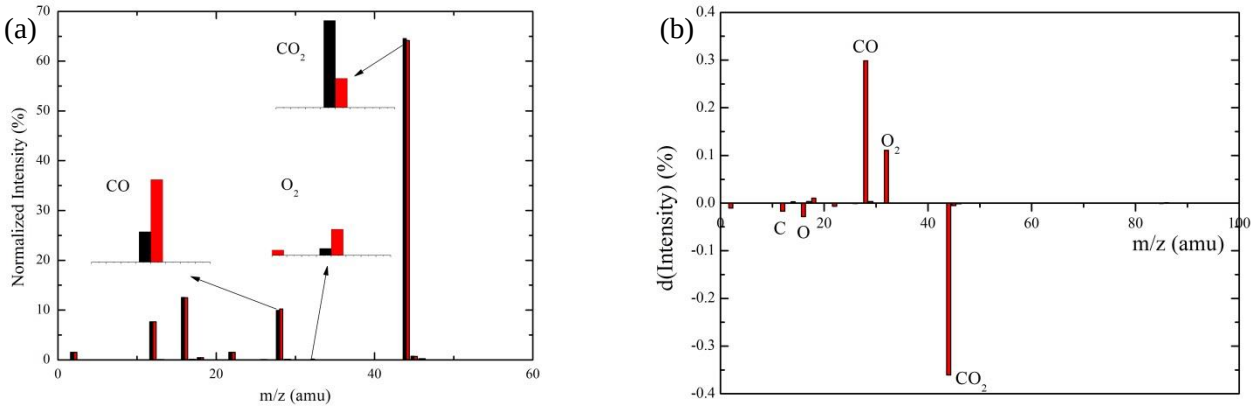

Figure 4.6. (a) The mass spectrum of inlet (black) and product (red) gases. The spectrum was normalized by the total ion current. (b) The difference in intensities between the inlet and product gases.

μ_{CO_2} is the molar mass of carbon dioxide. The mass spectra of the inlet and the product gases were measured by a quadrupole mass spectrometer, as depicted in Figure 3.5. The change in signal intensities can be seen after the device was turned on. The mass spectra of the gases before and after the operation of microplasma device are plotted in Figure 4.6 (a). Figure 4.6 (b) shows the difference in intensities of the inlet and the product gases ($I_f - I_i$). The result indicates that the purity of the input gas is well conserved until the gas reaches the vacuum chamber and that the microplasma devices are able to decompose carbon dioxide molecules into carbon monoxide

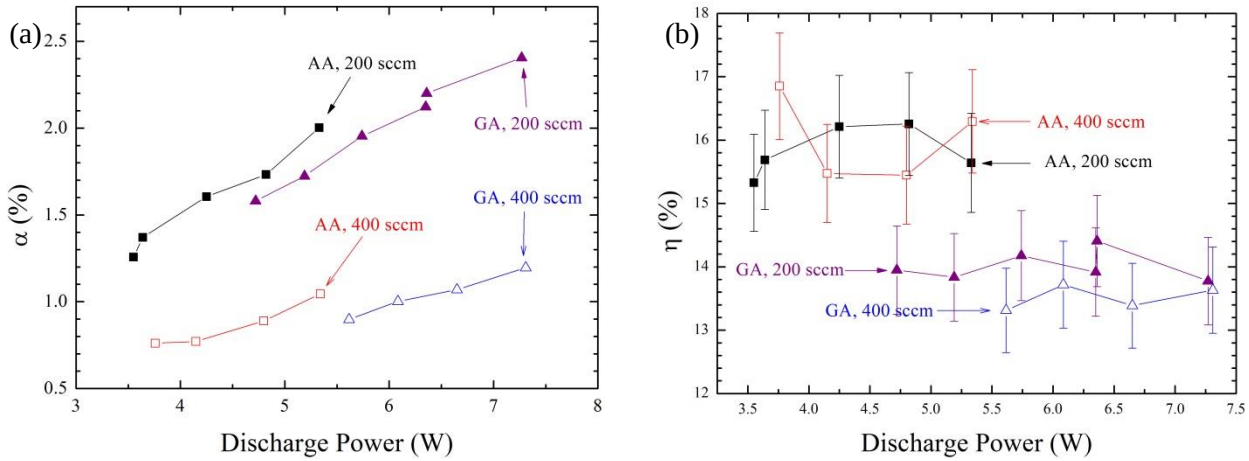

Figure 4.7. The conversion rate (a) and the energy efficiency (b) of each device at the standard volumetric flow rate of 200 sccm and 400 sccm.

and oxygen, as indicated by the stoichiometry in Equation (2.9).

The conversion rate and the energy efficiency of our devices were calculated by substituting measured values from mass spectroscopy into Equation (4.2), (4.3), and (4.5). The results were plotted in Figure 4.7 (a) and (b). The conversion rate showed a linear dependence on the discharge power. The conversion rate of 2.40 ± 0.1 % was achieved by the glass-alumina device at 200 sccm of flow rate. This value is lower than those found using other discharge methods such as microwave and radiofrequency plasmas [6, 19, 21]. Since there was no indication of the onset of saturation of the linear tendency, it can be expected that higher conversion rate will be achieved if more power is loaded to the devices. We can also increase the reaction volume by extending the length or the number of channels in an array. These will also result in a longer residence time of carbon dioxide molecules inside the reaction channels and more reactions will occur. This hypothesis is supported by the fact that a lower conversion rate was obtained with higher mass flow rates. The conversion rate increases with residing time until the residing time is long enough for the reactants to reach the equilibrium [6].

The energy efficiency of each device was quite steady in the given range of power loading as a result of linear dependence of the conversion rate on the discharge power. The alumina-alumina devices and the glass-alumina devices achieved 15.5 – 16.8 % and 13.5 – 14.4 % of energy efficiency, respectively. The energy efficiency of our microplasma devices was compared with other types of discharges in Table 4.4. The maximum value of energy efficiency was reported to be 90 % by Azizov's work (1983) using non-equilibrium microwave discharge at < 200 Torr of pressure under supersonic flow [10, 32]. Although the energy efficiency of low-pressure non-equilibrium high energy plasmas surpassed our values, when compared to

Table 4.4 Highest values of energy efficiencies that can be found in references for different types of discharges.

Discharge type	Energy efficiency (%)	Remarks
Theoretical maximum of thermal plasma (equilibrium)	48	[25]
Experimental quasi-thermal plasma (arc discharge)	15	[26]
Low pressure glow discharge	8	[27]
High-current relativistic electron beam	30	Atmospheric pressure [28]
Low-pressure plasma-beam discharge	50	[29]
Radiofrequency discharge	60	300 Torr [30]
Pulsed microwave discharge	60	300 Torr [31]
Pulsed microwave discharge	90	< 200 Torr, supersonic flow [32]
Dielectric barrier discharge	< 10	Atmospheric pressure, diluted in N_2, O_2, or Ar [3, 24]
Dielectric barrier discharge	2	[5]
Microplasma discharge	16	This work

analogous dielectric barrier atmospheric pressure plasmas, our devices showed better performance in terms of energy efficiency.

The energy yield has basically the same meaning as the energy efficiency except for a constant. Nevertheless, by expressing it with the units of g/kWh, we can compare the number to the breakeven point where the electricity generated by energy sources dissociates all carbon dioxide emitted from the electricity generation. For example, combustion of natural gas, gasoline, and coal emits 180, 240, and 320 g of carbon dioxide for 1 kWh of energy, respectively [1], and the breakeven point can be reached when those numbers of energy yields are achieved. Our energy efficiencies of 16 % and 14 % of energy efficiency for alumina-alumina devices and glass-alumina devices correspond to 90 g/kWh and 79 g/kWh of energy yield. If the energy yield can be increased to > 300 g/kWh, it will reach the breakeven point and the carbon dioxide emission by electricity generation can be significantly reduced using microplasma devices.

Another advantage of microplasma is the small volume. The total discharge volume of one alumina and glass microchannel with 30 mm length was only 1.8×10^{-2} cm^3, measured from microscope images. Consequently, an array of 12 microchannels as the devices used in our experiments gave total volume of 0.22 cm^3. By dividing the energy yield by the plasma volume, we suggest a new representation of carbon dioxide processing which will give a measure of the performance in unit volume of plasma system.

$$\mathrm{E}_{Y/V}(g/mL \cdot kWh) = \frac{\Delta \dot{m}_{CO_2}}{\mathrm{V} \times \mathrm{P}} \tag{4.6}$$

The energy yield per volume of microplasma reactors was about 400 g/mL-kWh.

4.4 Conclusion

In conclusion, the microplasma discharge of carbon dioxide was successfully operated in atmospheric pressure and low temperature condition using microchannel plasma devices. Among the four types of devices tested, the glass-alumina device and alumina-alumina devices were chosen for their stable operation at relatively high discharge power ~5 W. The optical emission spectrum of carbon dioxide plasma indicated that our microplasma system is able to excite or ionize carbon dioxide molecules and break the C-O double bond (Figure 4.3). The appearance of the C_2 Swan bands, the CO triplet bands, atomic oxygen peak, and the molecular ion peaks support this observation. Also, comparison of the optical emission spectra of pure argon and carbon dioxide to that of Ar-CO_2 mixture plasmas suggests the possibility of energy transfer between certain states of excited atomic argon and C_2 molecule. As a result of the plasma chemical reaction of carbon dioxide, carbon monoxide and oxygen was produced. The reaction

was quantitatively analyzed by a quadrupole mass spectrometer. 2.40 ± 0.1 % of conversion rate and 14.4 ± 0.5 % of energy efficiency was achieved by the glass-alumina devices, and 2.00 ± 0.1 % of conversion rate and 15.7 ± 0.5 % of energy efficiency was obtained by alumina-alumina microplasma devices, at the standard volumetric flow rate of 200 sccm.

Our microplasma devices showed several advantages in carbon dioxide dissociation over other comparable dielectric barrier discharges: low breakdown voltage, small plasma volume, and higher efficiency. Further optimization of device geometry, channel dimensions, flow rate, operation temperature, and addition of catalytic layers will be pursued to improve the performance of these devices.

REFERENCES

[1] U.S. Energy Information Administration. (2011). *Emissions of greenhouse gases in the U.S.* (OIG publication No. DOE/EIA-0573(2009)). Washington, DC: John Conti. Retrieved from http://www.eia.gov/environment/emissions/ghg_report/pdf/0573(2009).pdf

[2] U.S. Energy Information Administration. (2012). *Annual Energy Review* (OIG publication No. DOE/EIA-0384(2011)). Washington, DC: DOE. Retrieved from http://www.eia.gov/totalenergy/data/annual/pdf/aer.pdf

[3] Wang, S., Zhang, Y., Liu, X., & Wang, X. (2012). Enhancement of CO2 conversion rate and conversion efficiency by homogeneous discharges. *Plasma Chemistry and Plasma Processing*, *32*(5), 979-989. doi: 10.1007/s11090-012-9386-8

[4] Li, R., Tang, Q., Yin, S., & Sato, T. (2006). Plasma catalysis for CO2 decomposition by using different dielectric materials. *Fuel Processing Technology*, *87*(7), 617-622. doi: 10.1016/j.fuproc.2006.01.007

[5] Paulussen, S. , Verheyde, B., Tu, X., De Bie, C., Martens, T., Petrovic, D., Bogaerts, A., & Sels, B. (2010). Conversion of Carbon dioxide to value-added chemicals in atmospheric pressure dielectric barrier discharges. *Plasma Sources Science and Technology*, *19*(3), doi: 10.1088/0963-0252/19/3/034015

[6] Spencer, L., & Gallimore, A. (2011). Efficiency of CO2 dissociation in a radio-frequency discharge. *Plasma Chemistry and Plasma Processing*, *31*(1), 79-89. doi: 10.1007/s11090-010-9273-0

[7] Long, H., Shang, S., Tao, X., Yin, Y., & Dai, X. (2008). CO2 reforming of CH4 by combination of cold plasma jet and ni/γ-Al2O3 catalyst. *International Journal of Hydrogen Energy*, *33*(20), 5510-5515. doi: 10.1016/j.ijhydene.2008.05.026

[8] Becker, K. H., Schoenbach, K. H., & Eden, J. G. (2006). Microplasmas and applications. *Journal of Physics D: Applied Physics*, *39*(3), R55-R70. doi:10.1088/0022-3727/39/3/R01

[9] Lieberman, M. A., & Lichtenberg, A. J. (2005). *Principles of plasma discharges and materials processing* (2nd ed.). Hoboken, NJ: John Wiley & Sons, Inc.

[10] Fridman, A. (2008). *Plasma chemistry*. New York, NY: Cambridge University Press.

[11] Bogaerts, A., De Bie, C., Eckert, M., Georgieva, V., Martens, T., Neyts, E., & Tinck, S. (2010). Modeling of the plasma chemistry and plasma-surface interactions in reactive plasmas. *Pure and Applied Chemistry*, *82*(6), 1283-1299. doi:10.1351/PAC-CON-09-09-20

[12] Darwent, B. (1970). *Bond dissociation energies in simple molecules*. (Vol. 229, pp. 1-48). Washington D.C.: US National Bureau of Standards. Retrieved from http://www.nist.gov/data/nsrds/NSRDS-NBS31.pdf

[13] Park, S. -J., Kim, K. S., & Eden, J. G. (2005). Nanoporous alumina as a dielectric for microcavity plasma devices: Multilayer Al/Al_2O_3 structures. *Applied Physics Letters, 86*(22), 221501. doi: 10.1063/1.1923747

[14] Ko, S., Lee, D., Jee, S., Park, H., Lee, K., & Hwang, W. (2006). Mechanical properties and residual stress in porous anodic alumina structures. *Thin Solid Films, 515*(4), 1932-1937. doi: 10.1016/j.tsf.2006.07.169

[15] Ten Thige Boonkkamp, J. H. M., &Jansen, J. K. M. (2002). An analytical solution for mechanical etching of glass by powder blasting. *Journal of Engineering Mathmatics 43*, 385-399.

[16] Belloy, E., Thurre, S., Walckiers, E., Sayah, A., & Gijs, M. A. M. (2000). The introduction of powder blasting for sensor and microsystem applications. *Sensors and Actuators A: Physical, 84*(3), 330-337. doi: 10.1016/S0924-4247(00)00390-3

[17] Wefers, K., & Misra, C. (1987). Oxides and hydroxides of aluminum, *Alcoa Technical Paper, 19,* Alcoa Laboratories.

[18] Hagelsieb, M. L. (2007). *Anodic aluminum oxide processing, characterization and application to DNA hybridization electrical detection* (Doctoral dissertation). Universit é catholique de Louvain.

[19] Babou, Y., Riviere, P., Perrin, M. –Y., & Soufiani, A. (2008). Spectroscopic study of microwave plasmas of CO_2 and CO_2-N_2 mixtures at atmospheric pressure. *Plasma Sources Science and Technology, 17*(4), doi: 10.1088/0963-0252/17/4/045010

[20] Pearse, R. W. B., & Gaydon, A. G. (1965). *The identification of molecular spectra* (3rd ed.). London, UK: Whitefriars Press.

[21] Garcia-Cosio, G., Martinez, H., Calixto-Rodriguez, M., & Gomez, A. (2011). DC discharge experiment in an Ar/N2/CO2 ternary mixture: A laboratory simulation of the martian ionosphere's plasma environment. *Journal of Quantitative Spectroscopy and Radiative Transfer, 112*(18), 2787-2793. doi: 10.1016/j.jqsrt.2011.09.008

[22] Kramida, A., Ralchenko, Yu., Reader, J., & NIST ASD Team (2012). *NIST Atomic Spectra Database* (ver. 5.0), [Online]. Available: http://physics.nist.gov/asd [2013, April 11]. National Institute of Standards and Technology, Gaithersburg, MD.

[23] Rosenstock, H. M., Draxl, K., Steiner, B.W., & Herron, J.T. "Ion energetic data" in *NIST Chemistry WebBook, NIST Standard Reference Database Number 69*, Eds. P.J. Linstrom and W.G. Mallard, National Institute of Standards and Technology, Gaithersburg MD, 20899, http://webbook.nist.gov.

[24] Zheng, G., Jiang, J., W, Y., Zhang, R., & Hou, H. (2002). The mutual conversion of CO_2 and CO in dielectric barrier discharge (DBD). *Plasma Chemistry and Plasma Processing, 23*(1). 59-68.

[25] Butylkin, Yu. P., Grinenko, A. A., Levitskii, A. A., Polak, L. S., Rytova, N. M., & Slovetskii, D. I. (1979). Mathematical modeling of the kinetics of the thermal decomposition of carbon dioxide in an electric arc discharge and quenching of the product. *Soviet Physics, High Energy Chmistry, 13*(6). 545-551.

[26] Polak, L. S., Slovetsky, K. I., & Butylkin, Yu. P. (1977). *Carbon dioxide dissociation in electric discharges: arc discharge*. Moscow, RU: Institute of Petrochemical synthesis, USSR Academy of Sciences.

[27] Metel, A. S., & Nastukha, A. I. (1977). Decomposition of CO_2 in a glow discharge with a hollow cathode. *Soviet Physics, High Energy Chemistry, 11*(4), 366-370.

[28] Vakar, A. K., Denisenko, V. P., Maksimov, G. P., Rusanov, V. D., & Fridman, A. (1978). *The 3rd USSR Symposium on High Current Electronics*, Tomsk, RU.

[29] Nikiforov, V. A. (1979). *Experiments with plasma-beam discharge; chemically active plasma* (Doctoral dissertation). Kurchatov Institue of Atomic Energy.

[30] Butylkin, Yu. P., Givotov, V. K., Krasheninnikov, E. G., Krotov, M. F., Rusanov, V. D., Tarasov, Yu. V., & Fridman, A. A. (1981). Dissociation of CO_2 by a plasma-chemical process in a nonequilibrium microwave discharge. *Soviet Physics, Technical Physics, 26*(5), 555-558.

[31] Azizov, R. I., Zhivotov, V. K., & Rusanov, V. D. (1977). *The 3rd International Symposium on Plasma Chemistry*, Limoges, FR.

[32] Azizov, R. I., Vakar, A. K., Zhivotov, V. K., Krotov, M. F., Zhinov'ev, O. A., Potapkin, B. V., Rusanov, A. A., Rusanov, V. D., & Fridman, A. A. (1983). The nonequilibrium plasmachemical process of decomposition of CO_2 in a supersonic SHF discharge. *Soviet Physics, Doklady, 28*(7), 567-569.